

Coupled-channel analysis of the near-threshold $e^+e^- \rightarrow N\bar{N}$ cross sections

Zhao-Sai Jia^{1,2,*}, Zhen-Hua Zhang^{3,2,*}, Feng-Kun Guo^{2,4,5,6,†} and Gang Li^{1,‡}

¹*College of Physics and Engineering, Qufu Normal University, Qufu 273165, China*

²*CAS Key Laboratory of Theoretical Physics, Institute of Theoretical Physics,
Chinese Academy of Sciences, Beijing 100190, China*

³*School of Physics and Center of High Energy Physics, Peking University, Beijing 100871, China*

⁴*School of Physical Sciences, University of Chinese Academy of Sciences, Beijing 100049, China*

⁵*Peng Huanwu Collaborative Center for Research and Education, Beihang University, Beijing 100191, China*

⁶*Southern Center for Nuclear-Science Theory (SCNT), Institute of Modern Physics,
Chinese Academy of Sciences, Huizhou 516000, China*

The possible existence of nucleon-antinucleon bound states has been studied for decades. We investigate the $e^+e^- \rightarrow p\bar{p}$ and $e^+e^- \rightarrow n\bar{n}$ cross sections in the nonrelativistic effective field theory framework. The proton-antiproton and neutron-antineutron coupled-channel final state interactions are considered and found responsible for near-threshold enhancements. Both the proton-neutron mass difference and the Coulomb interaction between p and \bar{p} are considered, and the $N\bar{N}$ strong interactions are taken into account through a short-distance optical potential. By fitting the low energy constants in the amplitudes to the data for the near-threshold $e^+e^- \rightarrow N\bar{N}$ cross sections from the BESIII and SND Collaborations, a $N\bar{N}$ quasi-bound state is found just above the $p\bar{p}$ threshold, and another $N\bar{N}$ pole is found on the unphysical Riemann sheet, farther away from the threshold. The constructed coupled-channel amplitude with Coulomb effects also offers a framework that can be used directly in experimental analyses on fine structures near the $N\bar{N}$ thresholds.

I. INTRODUCTION

The interest on the nucleon-antinucleon bound states have been lasting for decades [1]. They are analogues of the deuteron but with a vanishing baryon number. One prominent candidate of a $p\bar{p}$ bound state is the $X(1835)$ observed in the $\eta'\pi^+\pi^-$ invariant mass distribution by the BES Collaboration [2] in the $J/\psi \rightarrow \gamma\eta'\pi^+\pi^-$ process in 2005. It could correspond to the near-threshold enhancement in the $p\bar{p}$ final state spectrum of the $J/\psi \rightarrow \gamma p\bar{p}$ decay observed by BES in 2003 [3]. The $X(1835)$ and the $p\bar{p}$ near-threshold enhancement were later confirmed by the BESIII [4, 5] and CLEO [6] experiments with higher statistics, and their quantum numbers were determined to be $J^{PC} = 0^{-+}$ [7, 8]. In 2013, a narrower structure $X(1840)$ with $J^{PC} = 0^{-+}$ was reported by BESIII in the 6π spectrum of the $J/\psi \rightarrow \gamma 3(\pi^+\pi^-)$ decay [9], and $X(1880)$ in the intermediate vicinity of the $p\bar{p}$ threshold was reported using the full data set of BESIII in 2024 [10]. The higher precision data for the $X(1835)$ and $X(1840)$ demonstrated line shapes distorted from the Breit-Wigner distribution, which could be attributed to the $p\bar{p}$ threshold effect or the interference between two resonances [10, 11]. On the other hand, no near-threshold enhancement was observed in the $J/\psi \rightarrow \omega p\bar{p}$ process [12]. Many theoretical efforts have been made to explain these

* These authors contributed equally to this work.

† fkguo@itp.ac.cn

‡ gli@qfmu.edu.cn

anomalous near-threshold structures. Besides the $p\bar{p}$ bound state [13–16] or the final state interaction (FSI) effect [17–22], the resonances were also interpreted as, e.g., pseudoscalar glueballs [23–27] and radial excitation states of the η' meson [28–30] (for reviews, see [31, 32]), while no consensus has been reached so far. $p\bar{p}$ near-threshold enhancements have also been observed in other processes, e.g., in the $p\bar{p}$ spectrum in the B decays [33–35] and $\psi(2S)$ decays [4, 6, 7], as well as in the $e^+e^- \rightarrow p\bar{p}$ process [36–38]. In particular, the enhancement in $e^+e^- \rightarrow p\bar{p}$ is of particular interest as it could contain the contribution of possible $N\bar{N}$ ($N = p, n$) vector bound state(s) with $J^{PC} = 1^{--}$.

The enhancement in $e^+e^- \rightarrow p\bar{p}$ has been known for a long time. In 1994, the PS170 Collaboration [39] first reported the steep energy dependence of the $p\bar{p} \rightarrow e^+e^-$ cross section near the $p\bar{p}$ threshold. The near-threshold enhancement was later confirmed by the FENICE Collaboration [40] in the cross section for $e^+e^- \rightarrow p\bar{p}$ with large uncertainties, and the first measurement of the $e^+e^- \rightarrow n\bar{n}$ cross section [41] was also made by the FENICE group. Since then, there have been updated measurements of the $e^+e^- \rightarrow N\bar{N}$ cross sections by the BaBar [36, 37], CMD-3 [38, 42], BESIII [43–47], and SND [48–50] Collaborations, providing more precise data near the $N\bar{N}$ thresholds. Particularly, the CMD-3 Collaboration measured the $e^+e^- \rightarrow p\bar{p}$ cross section and found that the steep rise happened within about 1 MeV above the $p\bar{p}$ threshold [42]. It has been shown that the near-threshold enhancement in the $e^+e^- \rightarrow p\bar{p}$ cross section can be explained by the FSI between the p and \bar{p} in a series of theoretical studies [51–57], where the $N\bar{N}$ interaction potential is given by models such as the Paris model [52, 58], Nijmegen model [59] and Jülich model [53, 60–63] or the chiral effective field theory [21, 63–65]. All these potentials are optical potentials [66], whose imaginary parts account for contributions from the strong annihilation channels of the $N\bar{N}$ far below the $N\bar{N}$ thresholds, e.g., $n\pi$ ($n \geq 2$), and these different models give similar results. However, most of these theoretical works ignored the Coulomb interaction between p and \bar{p} and the proton-neutron mass difference, as such effects should be sizeable only within a few MeV above the $p\bar{p}$ threshold while the data studied in the literature concentrated on a higher energy region. The first coupled-channel model including the Coulomb potential in the position space was given by Ref. [56] and improved in Ref. [57] to analyze the CMD-3 data with fine structures, and the model produced a clear cusp at the $n\bar{n}$ threshold. A pole about 4–20 MeV above the $p\bar{p}$ threshold with $I = 0$ and $^{(2S+1)}L_J = {}^3S_1$ (or 3S_1 – 3D_1 mixing) was found in the $N\bar{N}$ scattering matrix in many theoretical works [53–56, 63, 65]. Such a pole is located on the physical Riemann sheet (RS) of the complex energy plane and is referred as unstable or quasi-stable bound state in the literature. It is pushed away from the real axis to the complex energy plane by lower annihilation channels, and would become a bound state below the threshold when these annihilation channels are turned off [55, 65]. Recently, the SND Collaboration [50] has just released precise data for the $e^+e^- \rightarrow n\bar{n}$ near-threshold cross section, which offers great opportunities to study the possible near-threshold $N\bar{N}$ poles with $J^{PC} = 1^{--}$ in detail.

In this work, we investigate the $e^+e^- \rightarrow p\bar{p}$ and $e^+e^- \rightarrow n\bar{n}$ near-threshold cross sections in the nonrelativistic effective theory (NREFT) framework. The $N\bar{N}$ FSIs are taken into account in the Watson-Migdal approach [67, 68], including the $p\bar{p}$ – $n\bar{n}$ coupled-channel dynamics and the Coulomb interactions between p and \bar{p} . The leading order (LO) strong interaction between the N and \bar{N} is parametrized by a constant optical potential, and the corresponding low energy constants (LECs) are determined by a combined fit to the newly updated data for $e^+e^- \rightarrow n\bar{n}$ near-threshold cross sections from the SND Collaboration [50] and the $e^+e^- \rightarrow p\bar{p}$ near-threshold cross section measured by the BESIII Collaboration [46].

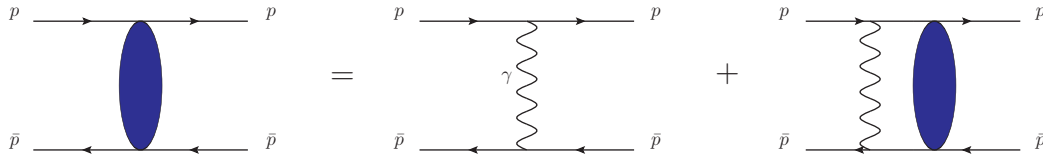


FIG. 1. Resummation in the Coulomb T -matrix for the $p\bar{p}$ scattering.

The near-threshold $N\bar{N}$ pole positions can then be derived.

The rest part of this paper is organized as follows. In Section II, we derive expressions for the $e^+e^- \rightarrow N\bar{N}$ cross sections in the coupled-channel NREFT. In Section III, the parameters are fixed by fitting to the experimental cross section data, and the pole positions of the $N\bar{N}$ coupled-channel scattering amplitudes in the near-threshold region are obtained with the fixed LECs. A brief summary is given in Section IV.

II. CROSS SECTIONS IN COUPLED-CHANNEL NREFT

In this section, we give the amplitudes and cross sections of $e^+e^- \rightarrow N\bar{N}$ near the $N\bar{N}$ thresholds in the $p\bar{p}$ - $n\bar{n}$ coupled-channel NREFT. The $p\bar{p}$ and $n\bar{n}$ are referred as the first and second channels, respectively. The two reactions $e^+e^- \rightarrow p\bar{p}$ and $e^+e^- \rightarrow n\bar{n}$ should proceed dominantly via the one-photon exchange [51, 53, 54], so the quantum numbers of the $N\bar{N}$ pair are fixed to be $J^{PC} = 1^{--}$. The near-threshold energy dependence of the cross sections is mainly given by that of the $N\bar{N}$ FSI amplitudes, which contain contributions from both Coulomb and strong interactions.

The transition operator of the $N\bar{N}$ scattering including the Coulomb contribution can be expressed in the two-potential formalism as [69]

$$\hat{T}(E) = \hat{T}_C(E) + \hat{G}_0(E)^{-1} \hat{G}_C(E) \hat{T}_{SC}(E) \hat{G}_C(E) \hat{G}_0(E)^{-1}, \quad (1)$$

where $E = \sqrt{s}$ is the total initial energy in the $N\bar{N}$ center-of-mass (c.m.) frame; \hat{T}_C and \hat{T}_{SC} are the Coulomb and strong-Coulomb transition operators, respectively; $\hat{G}_0 = 1/(E - \hat{H}_0 + i\varepsilon)$ is the free Green's resolvent with \hat{H}_0 the free Hamiltonian; and $\hat{G}_C = 1/(E - \hat{H}_0 - \hat{V}_C + i\varepsilon)$ the Coulomb Green's resolvent with \hat{V}_C the Coulomb potential. The transition operators satisfy the Lippmann-Schwinger equations (LSEs)

$$\hat{T}_C = \hat{V}_C + \hat{V}_C \hat{G}_0 \hat{T}_C, \quad (2)$$

$$\hat{T}_{SC} = \hat{V}_S + \hat{V}_S \hat{G}_C \hat{T}_{SC}, \quad (3)$$

where \hat{V}_S is the strong potential between N and \bar{N} .

The $N\bar{N}$ system with $J^{PC} = 1^{--}$ can only be in 3S_1 and 3D_1 partial waves [51]. We mainly consider the S -wave contribution in this work, as the near-threshold D -wave amplitude is suppressed by k_N^2 comparing to the S -wave one, with k_N the c.m. momentum of the nucleon N . The S -wave two-channel

scattering T -matrix reads [70, 71]

$$\mathbf{T}(E) = \begin{pmatrix} T_C(E) & 0 \\ 0 & 0 \end{pmatrix} + \begin{pmatrix} W_C(E) & 0 \\ 0 & 1 \end{pmatrix} \mathbf{T}_{SC}(E) \begin{pmatrix} W_C(E) & 0 \\ 0 & 1 \end{pmatrix}, \quad (4)$$

where

$$T_C(E) = \frac{\pi}{i\mu_p k_p} \left(\frac{\Gamma(1-ix)}{\Gamma(1+ix)} - 1 \right), \quad (5)$$

is the $p\bar{p}$ Coulomb scattering amplitude shown in Fig. 1 including infinite Coulomb photon exchanges, with $\mu_p = m_p/2$ the reduced mass of $p\bar{p}$, $k_p = \sqrt{2\mu_p(E-2m_p)}$ the c.m. momentum of the proton, $x = \alpha\mu_p/k_p$, and $\alpha = 1/137$ the fine-structure constant; the $\mathbf{T}_{SC}(E)$ is the strong-Coulomb scattering matrix; and

$$W_C(E) = \left(\frac{2\pi x}{1 - e^{-2\pi x}} \frac{\Gamma(1-ix)}{\Gamma(1+ix)} \right)^{1/2} \quad (6)$$

includes the effect of resumming the Coulomb photon exchanges between the $p\bar{p}$ pair in the initial or final state.

Since we focus on the immediate vicinity of the $N\bar{N}$ near-thresholds, it is reasonable to employ NREFT at LO, which has a constant strong interaction potential for the S wave. The scattering states in the two channels can be expressed in terms of the isospin basis as

$$\begin{aligned} |p\bar{p}\rangle &= -\frac{1}{\sqrt{2}} \left(|N\bar{N}, I=0\rangle + |N\bar{N}, I=1\rangle \right), \\ |n\bar{n}\rangle &= -\frac{1}{\sqrt{2}} \left(|N\bar{N}, I=0\rangle - |N\bar{N}, I=1\rangle \right), \end{aligned} \quad (7)$$

and the LO strong potential reads

$$\mathbf{V}_S = \frac{1}{2} \begin{pmatrix} C_{0N} + C_{1N} + \delta_{\text{em}} & C_{0N} - C_{1N} \\ C_{0N} - C_{1N} & C_{0N} + C_{1N} \end{pmatrix} \equiv \begin{pmatrix} a_1 + ia_2 & b_1 + ib_2 \\ b_1 + ib_2 & c_1 + ia_2 \end{pmatrix}, \quad (8)$$

where C_{0N} and C_{1N} are LECs for the isoscalar and isovector interactions, respectively, and δ_{em} represents electromagnetic and isospin breaking corrections on the $p\bar{p}$ strong interaction (see below) [71]. The \mathbf{V}_S matrix elements are complex valued, as reparametrized in terms of real free parameters $a_{1,2}$, $b_{1,2}$, and c_1 . The imaginary parts of the LECs account for the effects of the strong annihilation channels below the $N\bar{N}$ threshold [66]. Near the $N\bar{N}$ threshold, the energy dependence from these annihilation channels is smooth and thus can be approximated by constants at LO [72]. The LSE for the strong-Coulomb scattering amplitude \mathbf{T}_{SC} with the LO constant strong potential can be reduced to an algebraic equation

$$\begin{aligned} \mathbf{T}_{SC}(E) &= \mathbf{V}_S(\Lambda) + \mathbf{V}_S(\Lambda) \mathbf{G}_C(E, \Lambda) \mathbf{T}_{SC}(E) \\ &= [\mathbf{I} - \mathbf{V}_S(\Lambda) \mathbf{G}_C(E, \Lambda)]^{-1} \mathbf{V}_S(\Lambda), \end{aligned} \quad (9)$$

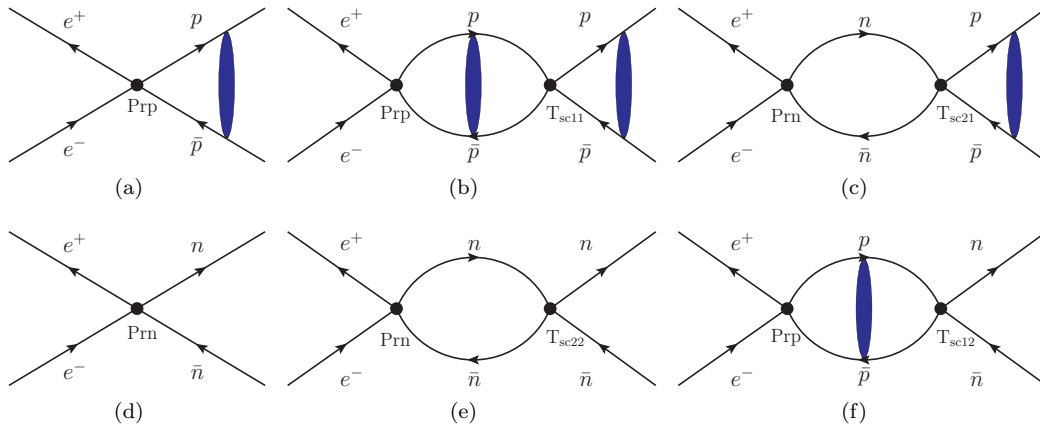


FIG. 2. Diagrams for the $e^+e^- \rightarrow p\bar{p}$ and $e^+e^- \rightarrow n\bar{n}$. The blue blob represents infinite Coulomb photon exchanges shown in Fig. 1.

where $\mathbf{G}_C(E, \Lambda) = \text{diag}(G_{C11}, G_{C22})$ is the Green's function regularized by a sharp cutoff Λ , with the nonvanishing diagonal matrix elements [69, 70, 73]

$$G_{C11}(E, \Lambda) = -\frac{\mu_p \Lambda}{\pi^2} - \frac{\alpha \mu_p^2}{\pi} \left(\ln \frac{\Lambda}{\alpha \mu_p} - \gamma_E \right) - \frac{\mu_p}{2\pi} \kappa_p(E), \quad (10)$$

$$G_{C22}(E, \Lambda) = -\frac{\mu_n \Lambda}{\pi^2} - i \frac{\mu_n}{2\pi} k_n(E), \quad (11)$$

where $\mu_n = m_n/2$ is the reduced mass of n and \bar{n} , γ_E is the Euler constant, $k_n = \sqrt{2\mu_n(E - 2m_n)}$ is the c.m. momentum of the neutron, and $\kappa_p = 2\alpha\mu_p [\ln(ix) + 1/(2ix) - \psi(-ix)]$ with $\psi(x)$ being the digamma function.

The Λ -dependence of \mathbf{G}_C can be absorbed into the potential \mathbf{V}_S through the renormalization procedure to achieve a cutoff-independent strong-Coulomb amplitude \mathbf{T}_{SC} , and the δ_{em} term in V_{S11} in Eq. (8) is utilized as a counterterm to absorb the logarithmic Λ term in Eq. (10) from electromagnetic corrections and the isospin breaking due to the difference between m_p and m_n . After renormalization, the \mathbf{T}_{SC} matrix can be expressed in terms of the Coulomb-modified scattering lengths $a_{ij}, i, j = 1, 2$ as [69]

$$\mathbf{T}_{SC}^{-1} = \mathbf{V}_S^{-1} - \mathbf{G}_C = \frac{1}{2\pi} \boldsymbol{\mu}^{1/2} \begin{pmatrix} -\frac{1}{a_{11}} & \frac{1}{a_{12}} \\ \frac{1}{a_{12}} & -\frac{1}{a_{22}} \end{pmatrix} \boldsymbol{\mu}^{1/2} - \mathbf{G}_C^R, \quad (12)$$

where $\boldsymbol{\mu} = \text{diag}(\mu_p, \mu_n)$, and

$$\mathbf{G}_C^R = \begin{pmatrix} -\frac{\mu_p}{2\pi} \kappa_p(E) & 0 \\ 0 & -\frac{i\mu_n}{2\pi} k_n(E) \end{pmatrix}, \quad (13)$$

is the renormalized Green's function.

The diagrams for the $e^+e^- \rightarrow p\bar{p}$ and $e^+e^- \rightarrow n\bar{n}$ processes are shown in Fig. 2. Since the $N\bar{N}$ pairs can be produced in S -wave, in the near-threshold region, the $N\bar{N}$ production vertices can be approximated by cutoff-dependent constants at LO, i.e., $\text{Prp}(\Lambda)$ and $\text{Prn}(\Lambda)$, for the $p\bar{p}$ and $n\bar{n}$ productions, respectively.

Consequently, the near-threshold production amplitudes for the $e^+e^- \rightarrow p\bar{p}$ and $e^+e^- \rightarrow n\bar{n}$ processes can be written as

$$\begin{aligned}\mathcal{M}[e^+e^- \rightarrow p\bar{p}] &= \text{Prp}(\Lambda) \times [1 + G_{C11}(\Lambda) \times T_{SC11}] \times W_C + \text{Prn}(\Lambda) \times G_{C22}(\Lambda) \times T_{SC21} \times W_C, \\ &= \text{Prp}(\Lambda) \times [1 + G_{C11}(\Lambda) \times T_{SC11} + R_{n/p} \times G_{C22}(\Lambda) \times T_{SC21}] \times W_C,\end{aligned}\quad (14)$$

$$\begin{aligned}\mathcal{M}[e^+e^- \rightarrow n\bar{n}] &= \text{Prn}(\Lambda) \times [1 + G_{C22}(\Lambda) \times T_{SC22}] + \text{Prp}(\Lambda) \times G_{C11}(\Lambda) \times T_{SC12} \\ &= \text{Prp}(\Lambda) \times [R_{n/p} + R_{n/p} \times G_{C22}(\Lambda) \times T_{SC22} + G_{C11}(\Lambda) \times T_{SC12}],\end{aligned}\quad (15)$$

where T_{SCij} are the T_{SC} matrix elements, and $R_{n/p} \equiv \text{Prn}/\text{Prp}$. The parameters Prp and Prn should be cutoff dependent, $\sim 1/\Lambda$, to absorb the Λ dependence in the intermediate Green's functions through the multiplicative renormalization [74]. Since we will use the full form of the above two amplitudes, subleading cutoff dependence exists from terms with solely Prp(Λ) and Prn(Λ) without Green's functions. We will take the cutoff Λ to be in the range between 2.0 and 2.6 GeV, large enough to serve as a hard scale, in the following analysis.

The BESIII [46] and SND [50] data for cross sections are fitted by

$$\sigma[e^+e^- \rightarrow p\bar{p}] = \frac{|\vec{p}_p|}{16\pi E^2 |\vec{p}_e|} |\mathcal{M}[e^+e^- \rightarrow p\bar{p}]|^2, \quad (16)$$

$$\sigma[e^+e^- \rightarrow n\bar{n}] = \frac{|\vec{p}_n|}{16\pi E^2 |\vec{p}_e|} |\mathcal{M}[e^+e^- \rightarrow n\bar{n}]|^2, \quad (17)$$

where $|\vec{p}_p|$ and $|\vec{p}_n|$ are the c.m. momenta of the final-state proton and neutron, respectively, and $|\vec{p}_e|$ is the c.m. momentum of the initial-state electron. There are seven free parameters in the fit: a_1 , a_2 , b_1 , b_2 , c_1 , Prp^2 , and $R_{n/p}$. The parameter space is constrained by unitarity, which requires the imaginary parts of the diagonal elements of the \mathbf{T} and \mathbf{V}_S matrices to be negative, i.e., $\text{Im}T_{ii} < 0$ and $a_2 < 0$ [75, 76].

III. RESULTS

In this section, we give the fitted near-threshold line shapes for the $N\bar{N}$ production cross sections and the poles of the $N\bar{N}$ scattering amplitudes. As the $p\bar{p}$ near-threshold production cross section data [46] are given in bins of the $p\bar{p}$ invariant mass and the width of each bin is about 25 MeV, the cross section in Eq. (16) is averaged for each bin to take the binning into account in our fit. The averaged $p\bar{p}$ and $n\bar{n}$ production cross sections in Eqs. (16) and (17) are utilized to simultaneously fit to the 5 datum points below 2.0 GeV given by BESIII [46] and the 13 data points below 1.91 GeV measured by the SND Collaboration [50], respectively. The momenta of the proton and neutron are smaller than 0.3 GeV, thus the NREFT treatment is well justified. We randomly generate 3×10^4 sets of initial values of the parameters constrained by unitarity to fit the data, and minimize the χ^2 function using the MINUIT algorithm [77–79].

We find two fits with similar quality, denoted as Fit 1 ($\chi^2/\text{d.o.f.} = 0.54$) and Fit 2 ($\chi^2/\text{d.o.f.} = 0.58$). They have the distinct features such that Fit 1 produces a sharp cusp at the $n\bar{n}$ threshold in the $p\bar{p}$ cross section and Fit 2 produces a bump between the $p\bar{p}$ and $n\bar{n}$ thresholds. The $n\bar{n}$ cross section line shapes are almost same in the two fits—there is no any prominent near-threshold peak but the cross section

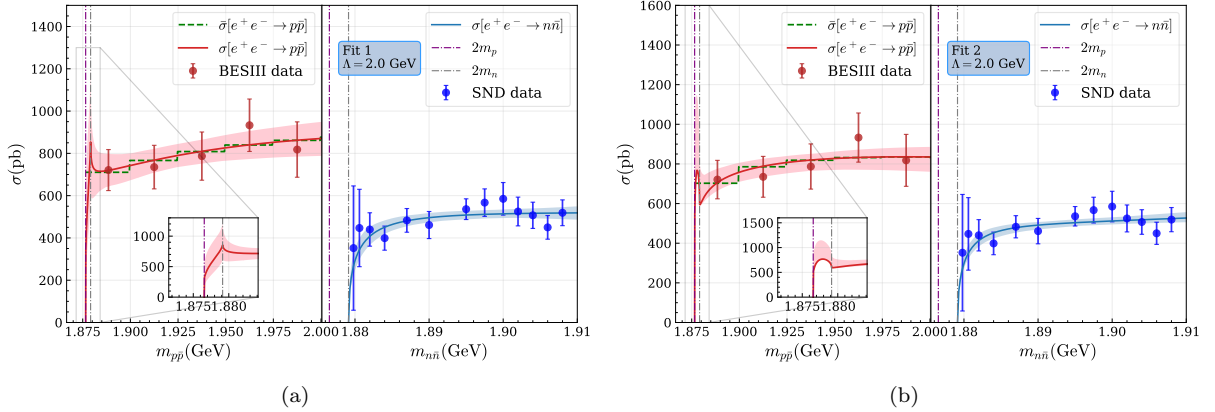


FIG. 3. Comparison between the best fitted cross sections in (a) Fit 1 and (b) Fit 2 for $e^+e^- \rightarrow p\bar{p}$ and $e^+e^- \rightarrow n\bar{n}$ with $\Lambda = 2.0$ GeV and the experimental data. The histograms (green dashed line) shows the best fits for $e^+e^- \rightarrow p\bar{p}$ with the cross sections averaged in each bin, and the red and blue solid curves are the corresponding continuous $e^+e^- \rightarrow p\bar{p}$ and $e^+e^- \rightarrow n\bar{n}$ cross sections, respectively. The bands are the 1σ error regions. The subplots enlarge the $e^+e^- \rightarrow p\bar{p}$ line shapes in the very near-threshold region. The vertical dot-dashed lines denote the $p\bar{p}$ (purple) and $n\bar{n}$ (gray) thresholds. The data points with error bars are taken from Table 4 in Ref. [46] for $e^+e^- \rightarrow p\bar{p}$ and Table I in Ref. [50] for $e^+e^- \rightarrow n\bar{n}$.

TABLE I. Scattering lengths obtained with $\Lambda = 2.0$ GeV. The uncertainties are the 1σ errors propagated from the statistical errors of the data.

Fit	a_{11} [fm]	a_{12} [fm]	a_{22} [fm]
1	$-0.25_{-0.01}^{+0.01} + i(0.03_{-0.01}^{+0.01})$	$0.28_{-0.01}^{+0.01} - i(0.00_{-0.01}^{+0.01})$	$-0.29_{-0.02}^{+0.01} + i(0.03_{-0.01}^{+0.01})$
2	$-0.29_{-0.01}^{+0.00} + i(0.02_{-0.00}^{+0.00})$	$0.33_{-0.01}^{+0.00} + i(0.00_{-0.00}^{+0.00})$	$-0.31_{-0.01}^{+0.00} + i(0.03_{-0.00}^{+0.01})$

rises immediately above threshold to give an almost flat distribution, which differs from the phase space distribution drastically. The best fitted line shapes for Λ varying between 2.0 and 2.6 GeV are almost the same. A comparison of the best fits with the experimental data for $\Lambda = 2.0$ GeV is shown in Fig. 3. The near-threshold data are well described by our coupled-channel formalism. The fitted line shapes with different Λ and the corresponding fitted parameters can be found in Appendix A. The Coulomb-modified scattering lengths in Eq. (12) obtained with $\Lambda = 2.0$ GeV extracted from the fits are listed in Table I, and the Λ dependence are shown in Fig. 4. The changes in the scattering lengths as Λ varying from 2.0 to 2.6 GeV is about 20%, which is indeed subleading as expected. The difference between the values of a_{11} and a_{22} is due to isospin breaking effects.

Although the magnitudes of the scattering lengths a_{11} and a_{22} are small, the large $1/|a_{12}| \gg \sqrt{2m_p(m_n - m_p)}$ indicates strong channel coupling and thus the possible near-threshold $N\bar{N} \ ^3S_1$ resonant states [80]. These resonant states appear as poles on the RSs of the complex energy E plane for the $T_{SC}(E)$ matrix in Eq. (9).

We find two near-threshold poles for both Fit 1 and Fit 2. One pole is located on the first (physical) RS (RS_{++}), and the other one is on the second RS (RS_{-+}), where $RS_{\pm\pm}$ is quoted to indicate the RSs where the poles are located, with the first and second signs in the subscript representing the signs of $\text{Im}k_p$ and $\text{Im}k_n$, respectively. The pole on the RS_{++} also has a shadow pole [81] on RS_{+-} , which is far from the physical region and will not be discussed in the following. The uncertainty of the pole positions

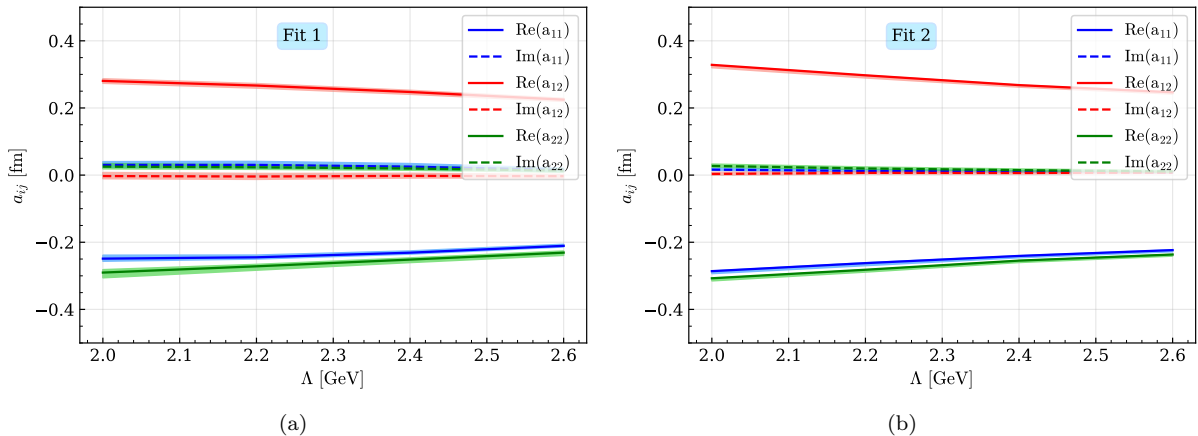


FIG. 4. Scattering length as a function of Λ extracted from (a) Fit 1 and (b) Fit 2.

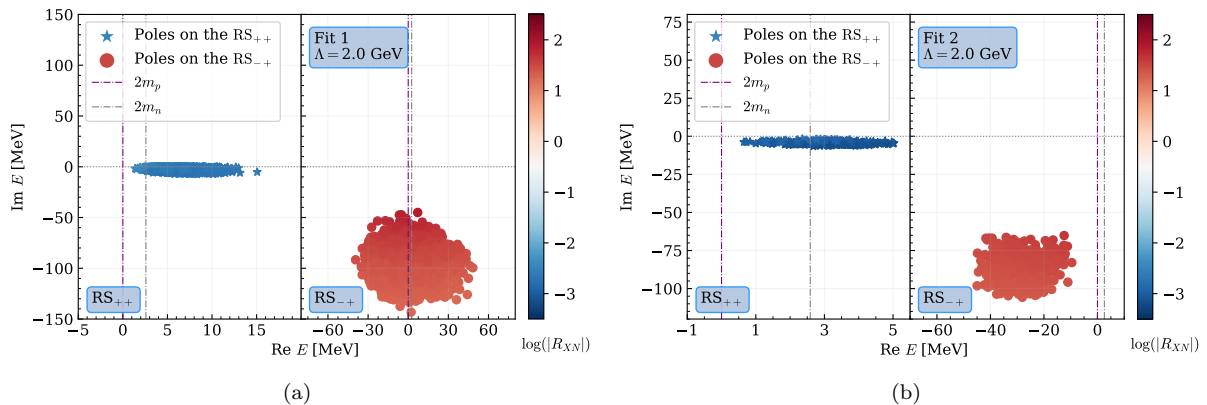


FIG. 5. Pole positions on the first and second RSs from (a) Fit 1 and (b) Fit 2 using parameters in the 1σ error range for $\Lambda = 2.0$ GeV. The logarithm of the absolute value of ratio between the isovector and isoscalar residues of each pole, $R_{XN} = g_{X,I=1}/g_{X,I=0}$, is encoded in color.

for each fit is computed using 3×10^4 parameter sets within the 1σ error region for $\Lambda = 2.0 - 2.6$ GeV, and the results for $\Lambda = 2.0$ GeV are shown in Fig. 5.

The pole positions for different Λ values are similar, as listed in Table II, where E_1 and E_2 denote the positions of the poles on the first and second RSs, respectively. For comparison, the pole positions with different Λ for Fit 1 and Fit 2 are given in Figs. 8 and 9, respectively, in Appendix A. Taking the uncertainties of the pole positions to cover the variations with $\Lambda \in [2.0, 2.6]$ GeV and the mean values of the central values listed in Table II as the central values, we obtain for Fit 1

$$E_1 = 1882.2^{+9.4}_{-4.5} - i(1.2^{+6.3}_{-1.2}) \text{ MeV}, \quad E_2 = 1882.2^{+79.4}_{-46.5} - i(106.4^{+83.5}_{-65.1}) \text{ MeV}, \quad (18)$$

and for Fit 2

$$E_1 = 1878.2^{+4.5}_{-1.0} - i(5.9^{+1.5}_{-4.7}) \text{ MeV}, \quad E_2 = 1817.7^{+53.1}_{-13.1} - i(99.4^{+46.7}_{-34.2}) \text{ MeV}. \quad (19)$$

The pole on RS_{++} in both fits is rather close to the $p\bar{p}$ threshold at 1876.27 MeV and $n\bar{n}$ threshold at 1879.13 MeV, with the one in Fit 1 above the $n\bar{n}$ threshold and the one in Fit 2 between the two

TABLE II. Pole positions with different Λ . E_1 and E_2 represent the pole positions on the RS_{++} and RS_{-+} , respectively. The uncertainties are the 1σ errors propagated from the statistical uncertainties of the data.

Λ [GeV]	Fit	E_1 [MeV](RS_{++})	E_2 [MeV](RS_{-+})
2.0	1	$1882.1^{+9.5}_{-4.2} - i(2.0^{+5.5}_{-2.0})$	$1877.3^{+47.5}_{-40.1} - i(89.3^{+53.8}_{-44.3})$
	2	$1877.7^{+3.9}_{-0.5} - i(5.8^{+0.9}_{-4.1})$	$1826.3^{+40.6}_{-5.2} - i(84.1^{+21.7}_{-18.9})$
2.2	1	$1882.1^{+7.6}_{-4.4} - i(1.2^{+5.4}_{-1.2})$	$1879.3^{+64.2}_{-42.6} - i(100.0^{+57.9}_{-58.7})$
	2	$1878.1^{+4.1}_{-0.9} - i(5.9^{+1.2}_{-4.7})$	$1822.1^{+48.7}_{-1.2} - i(93.6^{+26.2}_{-20.7})$
2.4	1	$1882.2^{+9.2}_{-4.5} - i(0.8^{+5.0}_{-0.8})$	$1883.0^{+71.6}_{-47.3} - i(111.5^{+67.5}_{-56.2})$
	2	$1878.3^{+3.8}_{-1.1} - i(5.9^{+1.2}_{-4.3})$	$1813.3^{+52.1}_{-0.0} - i(105.0^{+27.3}_{-23.9})$
2.6	1	$1882.4^{+7.7}_{-3.8} - i(0.6^{+4.9}_{-0.6})$	$1889.2^{+72.4}_{-51.9} - i(124.7^{+65.2}_{-59.9})$
	2	$1878.7^{+4.0}_{-1.5} - i(6.0^{+1.4}_{-4.6})$	$1809.2^{+57.3}_{-4.6} - i(114.8^{+31.3}_{-27.6})$

thresholds. Such difference in pole locations causes the different behaviors of the $p\bar{p}$ cross section near the $n\bar{n}$ threshold in the two fits [80]. The pole would become a bound state pole below the $p\bar{p}$ threshold without an imaginary part if the lower annihilation channels are turned off [55, 65].

The pole on RS_{-+} is much deeper in the complex plane compared with the one on RS_{++} , and has smaller impact on the line shapes, thus bearing larger uncertainties from fitting to line shape data. One also notices that the pole location differs significantly in the two fits, with the one in Fit 2 farther away from the thresholds than that in Fit 1.

Since the isospin of $N\bar{N}$ system can be either 0 or 1, the existence of two distinct poles at LO of NREFT indicates the presence of one isoscalar and one isovector $N\bar{N}$ molecular states. This expectation is confirmed by the couplings of the poles to the isoscalar and isovector channels. The effective couplings of the two near-threshold resonant states to $N\bar{N}$ can be derived from the residues of the \mathbf{T} matrix at the corresponding pole positions as

$$g_{Xi}g_{Xj} = \lim_{E \rightarrow E_X} (E - E_X)T_{ij}(E) \quad (20)$$

where $X = 1, 2$ correspond to the two poles on the first and second RSs, respectively, and $i, j = 1, 2$ are the channel indices. The couplings to the $I = 0, 1$ channels for the state corresponding to the pole X are

$$g_{X,I=0} = -\frac{1}{\sqrt{2}}(g_{X1} + g_{X2}), \quad g_{X,I=1} = -\frac{1}{\sqrt{2}}(g_{X1} - g_{X2}). \quad (21)$$

The magnitude of the ratio $R_{XN} \equiv g_{X,I=1}/g_{X,I=0}$ measures the relative strength between couplings for the X state to the isovector and isoscalar channels. The $\log(|R_{XN}|)$ value is encoded in colors in Fig. 5 (see also Figs. 8 and 9 in Appendix A).

For the pole on RS_{++} , the absolute value of its coupling to the isoscalar channel is about two to three orders of magnitude larger than that to the isovector channel. Therefore, the state is predominantly an isoscalar state, which is consistent with the previous studies [53–56, 63, 65].

The pole on RS_{-+} couples stronger to the isovector channel, as its coupling to the isovector channel

is about one to two orders of magnitude larger than that to the isoscalar channel. Previous studies also did not find any bound states in the isovector channel [53–56, 63, 65]. Our result that the isovector pole is on RS_{-+} instead of RS_{++} is consistent with these studies.

IV. SUMMARY

In this work, we studied the most updated data of the near-threshold $e^+e^- \rightarrow p\bar{p}$ and $e^+e^- \rightarrow n\bar{n}$ cross sections reported by the BESIII [46] and SND [50] Collaborations in the NREFT framework at LO. The framework includes both the $p\bar{p}$ and $n\bar{n}$ channels, with isospin breaking from the proton-neutron mass difference and the Coulomb interactions between p and \bar{p} .

We found two fits with similar quality that can well describe the near-threshold experimental cross sections. The line shape of the $p\bar{p}$ production cross section has a sharp cusp at the $n\bar{n}$ threshold for Fit 1 and a bump between the $p\bar{p}$ and $n\bar{n}$ thresholds for Fit 2. The Coulomb-modified scattering lengths [69] for the $p\bar{p}$ - $n\bar{n}$ coupled channels were obtained, and the results indicated a strong channel coupling [80]. Using the LECs determined from the fits, we studied possible $N\bar{N}$ composite states in the 3S_1 partial wave, which appear as poles of the strong-Coulomb T_{SC} matrix. As a consequence of the strong $p\bar{p}$ - $n\bar{n}$ channel coupling, two different poles exist in the orthogonal isoscalar and isovector channels. We obtained an isoscalar near-threshold $N\bar{N}$ quasi-bound state pole on the physical RS (RS_{++}), which lies either above the $n\bar{n}$ threshold (in Fit 1) or between the $p\bar{p}$ and $n\bar{n}$ thresholds (in Fit 2). We also found an isovector pole on the unphysical RS_{-+} . It is at least a few tens of MeV away from the $N\bar{N}$ thresholds, but its position is not well determined, differing sizeably between the two fits and bearing a large uncertainty.

Our results update the understanding on the near-threshold structures in the $e^+e^- \rightarrow N\bar{N}$ cross sections and the possible isoscalar and isovector $N\bar{N}$ composite states with $J^{PC} = 1^{--}$.

The amplitudes we derived for the $N\bar{N}$ FSIs can also be used in analyzing near-threshold data in other processes, such as $J/\psi \rightarrow \gamma p\bar{p}$ [3, 4], $B^\pm \rightarrow K^\pm p\bar{p}$ decays [33–35], and so on.

V. ACKNOWLEDGMENTS

We would like to thank Yan-Ping Huang who encouraged us to perform this study. This work is supported in part by the Chinese Academy of Sciences under Grants No. XDB34030000 and No. YSBR-101; by the National Key R&D Program of China under Grant No. 2023YFA1606703; by the National Natural Science Foundation of China (NSFC) under Grants No. 12125507, No. 12047503, No. 12475081, No. 12075133, and No. 12361141819; by the Natural Science Foundation of Shandong province under the Grant No. ZR2022ZD26; and by Taishan Scholar Project of Shandong Province under Grant No. tsqn202103062.

Appendix A: Fitted results with $\Lambda = 2.0 - 2.6$ GeV

In this appendix, we give the fitted parameter sets, line shapes of the cross sections and the pole positions for Fit 1 and Fit 2 with $\Lambda = 2.0 - 2.6$ GeV.

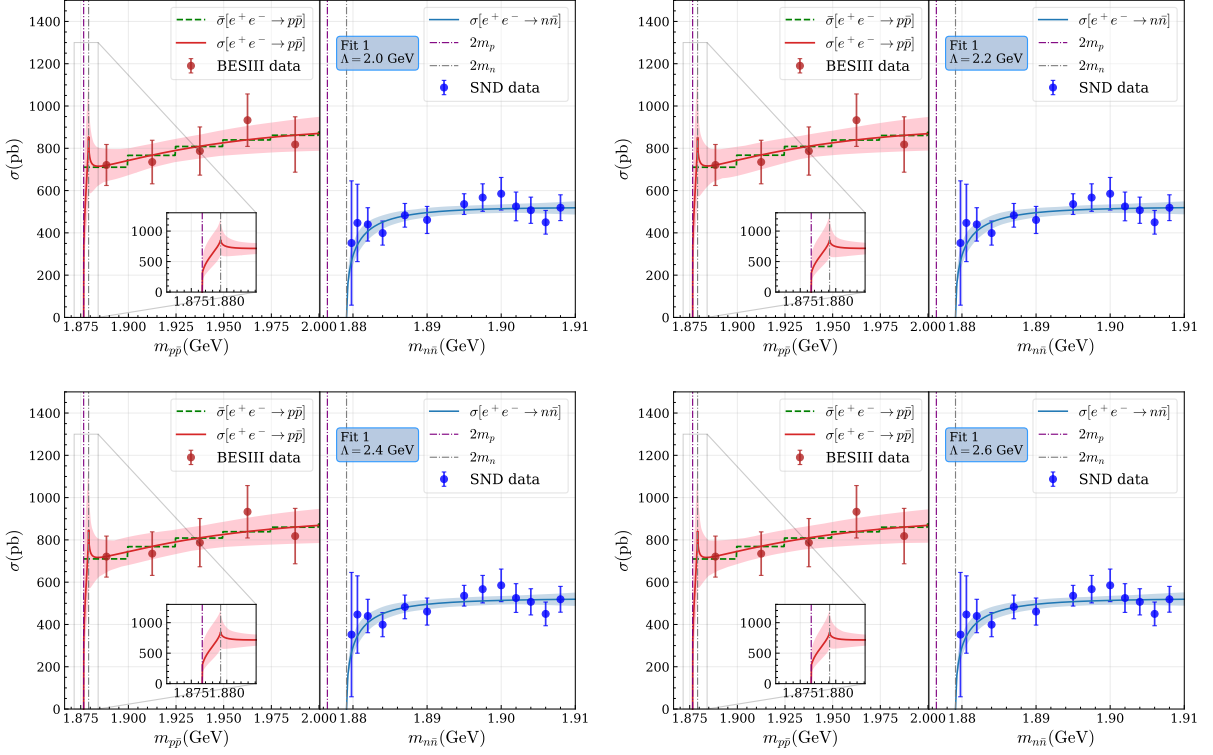


FIG. 6. Comparison of Fit 1 with different Λ values with the experimental data for $e^+e^- \rightarrow p\bar{p}$ [46] and $e^+e^- \rightarrow n\bar{n}$ [50]. The notations of the lines are same as in Fig. 3.

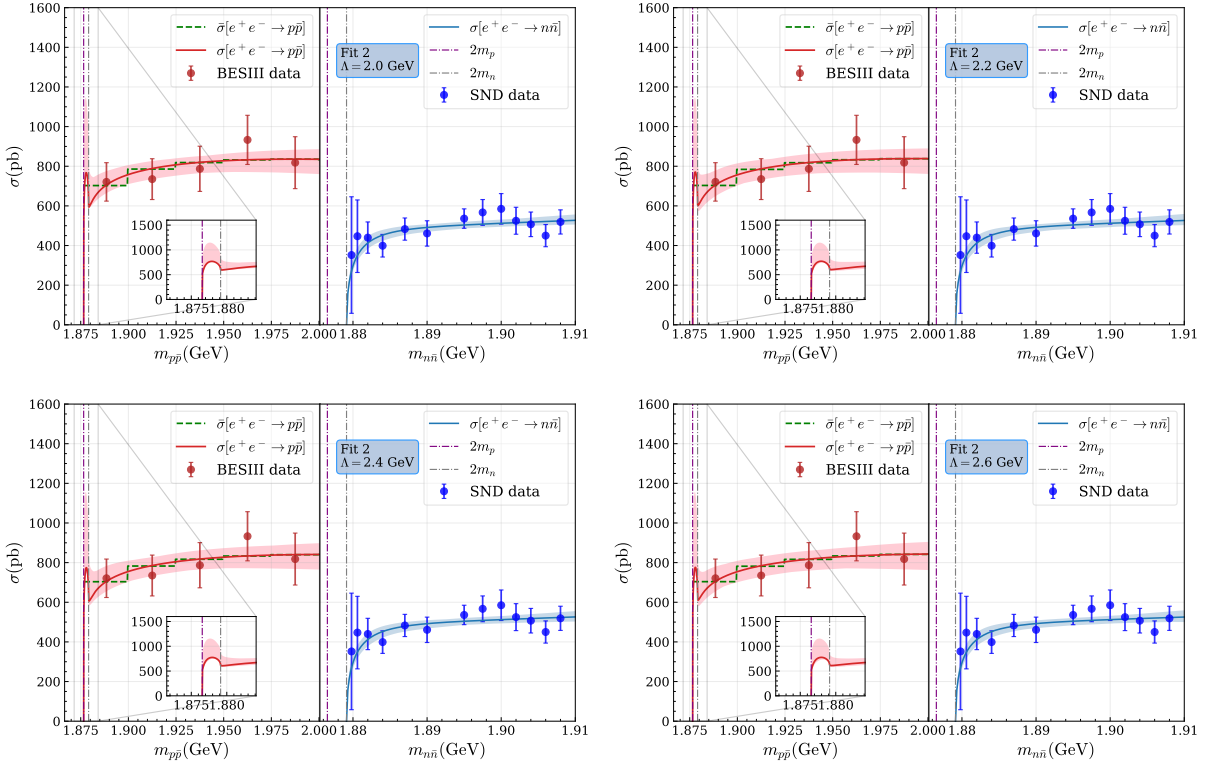


FIG. 7. Comparison of Fit 2 with different Λ values with the experimental data for $e^+e^- \rightarrow p\bar{p}$ [46] and $e^+e^- \rightarrow n\bar{n}$ [50]. The notations of the lines are same as in Fig. 3.

TABLE III. Parameter sets from Fit 1 with different Λ values. The uncertainties are the 1σ errors propagated from the statistical uncertainties of the data.

Λ [GeV]	$\chi^2/\text{d.o.f.}$	a_1 [fm ²]	a_2 [fm ²]	b_1 [fm ²]	b_2 [fm ²]	c_1 [fm ²]	Prp ²	$R_{n/p}$
2.0	0.54	$1.26^{+0.09}_{-0.07}$	$-0.85^{+0.06}_{-0.06}$	$1.57^{+0.06}_{-0.07}$	$-0.83^{+0.06}_{-0.06}$	$1.06^{+0.07}_{-0.10}$	$0.06^{+0.02}_{-0.02}$	$0.99^{+0.01}_{-0.02}$
2.2	0.54	$1.28^{+0.06}_{-0.06}$	$-1.69^{+0.04}_{-0.05}$	$1.57^{+0.06}_{-0.05}$	$-1.67^{+0.04}_{-0.05}$	$1.13^{+0.07}_{-0.08}$	$0.12^{+0.04}_{-0.03}$	$0.99^{+0.01}_{-0.01}$
2.4	0.54	$1.36^{+0.05}_{-0.05}$	$-2.06^{+0.03}_{-0.04}$	$1.63^{+0.06}_{-0.05}$	$-2.04^{+0.03}_{-0.03}$	$1.23^{+0.07}_{-0.07}$	$0.18^{+0.06}_{-0.05}$	$1.00^{+0.00}_{-0.01}$
2.6	0.54	$2.15^{+0.05}_{-0.04}$	$-1.10^{+0.03}_{-0.03}$	$2.40^{+0.04}_{-0.05}$	$-1.09^{+0.03}_{-0.03}$	$2.02^{+0.06}_{-0.08}$	$0.21^{+0.07}_{-0.06}$	$0.99^{+0.01}_{-0.01}$

TABLE IV. Parameter sets from Fit 2 with different Λ values. The uncertainties are the 1σ errors propagated from the statistical uncertainties of the data.

Λ [GeV]	$\chi^2/\text{d.o.f.}$	a_1 [fm ²]	a_2 [fm ²]	b_1 [fm ²]	b_2 [fm ²]	c_1 [fm ²]	Prp ²	$R_{n/p}$
2.0	0.58	$-3.30^{+0.07}_{-0.06}$	$-4.13^{+0.04}_{-0.04}$	$-2.79^{+0.07}_{-0.07}$	$-4.12^{+0.03}_{-0.04}$	$-3.12^{+0.08}_{-0.08}$	$0.54^{+0.10}_{-0.09}$	$0.99^{+0.00}_{-0.00}$
2.2	0.58	$-4.98^{+0.07}_{-0.05}$	$-3.81^{+0.04}_{-0.04}$	$-4.51^{+0.06}_{-0.06}$	$-3.80^{+0.04}_{-0.04}$	$-4.80^{+0.06}_{-0.07}$	$0.88^{+0.21}_{-0.19}$	$0.99^{+0.00}_{-0.00}$
2.4	0.58	$-5.62^{+0.06}_{-0.06}$	$-7.14^{+0.03}_{-0.03}$	$-5.21^{+0.05}_{-0.07}$	$-7.12^{+0.03}_{-0.03}$	$-5.49^{+0.06}_{-0.06}$	$2.30^{+0.52}_{-0.45}$	$1.00^{+0.00}_{-0.00}$
2.6	0.58	$-10.72^{+0.04}_{-0.04}$	$-5.65^{+0.03}_{-0.03}$	$-10.32^{+0.04}_{-0.05}$	$-5.64^{+0.03}_{-0.03}$	$-10.57^{+0.05}_{-0.06}$	$4.68^{+1.03}_{-1.04}$	$1.00^{+0.00}_{-0.00}$

The fitted line shapes of the near-threshold cross sections with different Λ values for Fit 1 and Fit 2, in comparison with the experimental data, are shown in Figs. 6 and 7, respectively. The line shapes are almost identical for different Λ and show the same behavior as discussed in the main text.

The parameter sets for Fit 1 and Fit 2 with different values of Λ are listed in Tables III and IV, respectively. For both fits, a_2 is constrained by unitarity to be negative, and b_2 as the imaginary part of the off-diagonal elements of the \mathbf{V}_S matrix is also negative. a_1 , b_1 and c_1 are positive for Fit 1 and negative for Fit 2. For both fits, the difference between a_1 and c_1 is small (less than 20% in Fit 1 and less than 5% in Fit 2), meaning that the isospin breaking effects are subleading. The short distance production sources for the $p\bar{p}$ and $n\bar{n}$ are almost identical, as their ratio $R_{n/p} \simeq 1$ in both fits.

The near-threshold pole positions of the \mathbf{T}_{SC} matrix with different Λ values for Fit 1 and Fit 2 are shown in Figs. 8 and 9, respectively. Their features have been discussed in the main text.

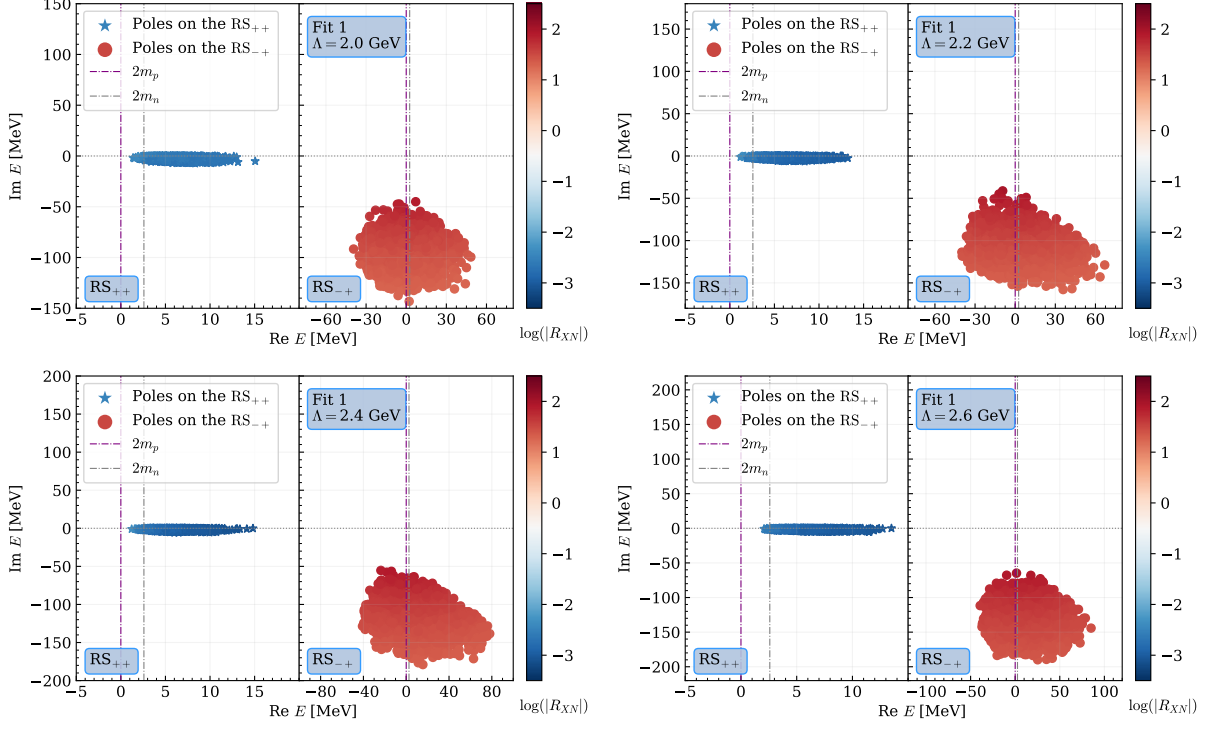


FIG. 8. Pole positions from Fit 1 with different Λ values using parameters in the 1σ error range. The color coding is same as Fig. 5.

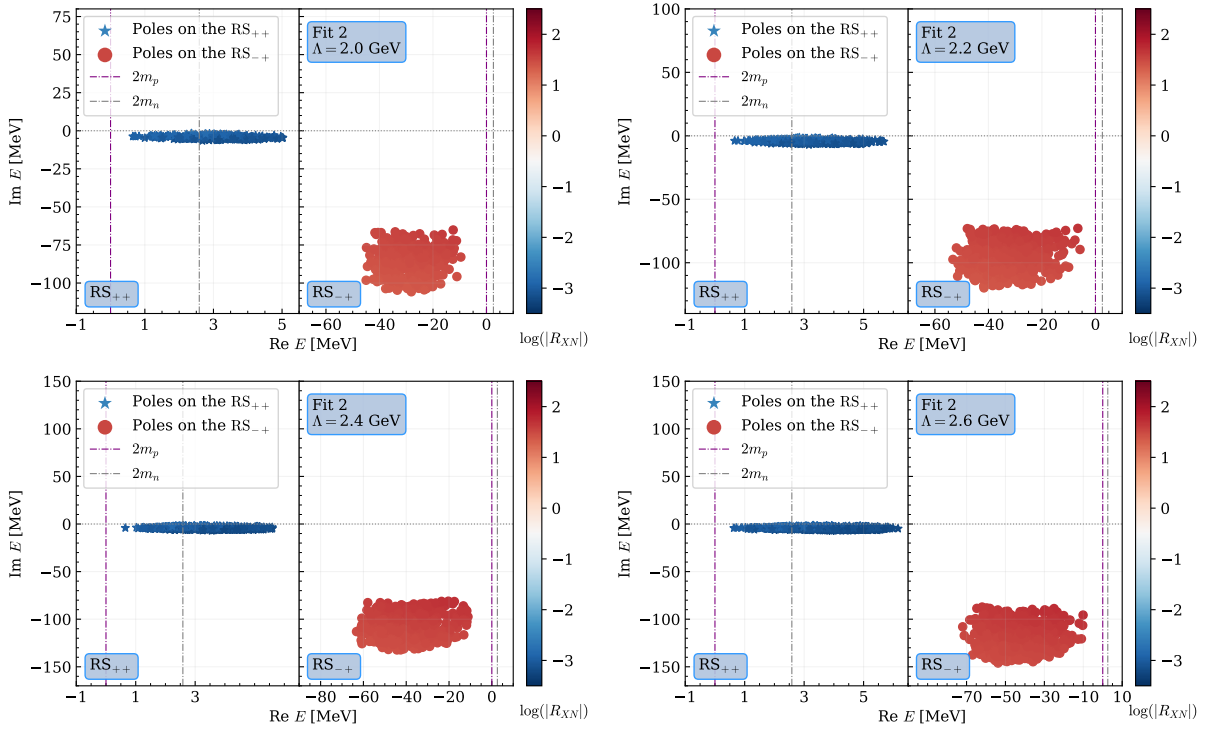


FIG. 9. Pole positions from Fit 2 with different Λ values using parameters in the 1σ error range. The color coding is same as Fig. 5.

-
- [1] E. Klempt, F. Bradamante, A. Martin, and J.-M. Richard, Antinucleon–nucleon interaction at low energy: scattering and protonium, *Phys. Rept.* **368**, 119 (2002).
- [2] M. Ablikim *et al.* (BES), Observation of a resonance X(1835) in $J/\psi \rightarrow \gamma\pi^+\pi^-\eta'$, *Phys. Rev. Lett.* **95**, 262001 (2005), arXiv:hep-ex/0508025.
- [3] J. Z. Bai *et al.* (BES), Observation of a near threshold enhancement in the $p\bar{p}$ mass spectrum from radiative $J/\psi \rightarrow \gamma p\bar{p}$ decays, *Phys. Rev. Lett.* **91**, 022001 (2003), arXiv:hep-ex/0303006.
- [4] M. Ablikim *et al.* (BESIII), Observation of a $p\bar{p}$ mass threshold enhancement in $\psi' \rightarrow \pi^+\pi^- J/\psi$ ($J/\psi \rightarrow \gamma p\bar{p}$) decay, *Chin. Phys. C* **34**, 421 (2010), arXiv:1001.5328 [hep-ex].
- [5] M. Ablikim *et al.* (BESIII), Confirmation of the X(1835) and observation of the resonances X(2120) and X(2370) in $J/\psi \rightarrow \gamma\pi^+\pi^-\eta'$, *Phys. Rev. Lett.* **106**, 072002 (2011), arXiv:1012.3510 [hep-ex].
- [6] J. P. Alexander *et al.* (CLEO), Study of $\psi(2S)$ Decays to $\gamma p\bar{p}$, $\pi^0 p\bar{p}$ and $\eta p\bar{p}$ and Search for $p\bar{p}$ Threshold Enhancements, *Phys. Rev. D* **82**, 092002 (2010), arXiv:1007.2886 [hep-ex].
- [7] M. Ablikim *et al.* (BESIII), Spin-Parity Analysis of $p\bar{p}$ Mass Threshold Structure in J/ψ and ψ' Radiative Decays, *Phys. Rev. Lett.* **108**, 112003 (2012), arXiv:1112.0942 [hep-ex].
- [8] M. Ablikim *et al.* (BESIII), Observation and Spin-Parity Determination of the X(1835) in $J/\psi \rightarrow \gamma K_S^0 K_S^0 \eta$, *Phys. Rev. Lett.* **115**, 091803 (2015), arXiv:1506.04807 [hep-ex].
- [9] M. Ablikim *et al.* (BESIII), Observation of a structure at 1.84 GeV/ c^2 in the $3(\pi^+\pi^-)$ mass spectrum in $J/\psi \rightarrow \gamma 3(\pi^+\pi^-)$ decays, *Phys. Rev. D* **88**, 091502 (2013), arXiv:1305.5333 [hep-ex].
- [10] M. Ablikim *et al.* (BESIII), Observation of the Anomalous Shape of X(1840) in $J/\psi \rightarrow \gamma 3(\pi^+\pi^-)$ Indicating a Second Resonance Near $p\bar{p}$ Threshold, *Phys. Rev. Lett.* **132**, 151901 (2024), arXiv:2310.17937 [hep-ex].
- [11] M. Ablikim *et al.* (BESIII), Observation of an anomalous line shape of the $\eta'\pi^+\pi^-$ mass spectrum near the $p\bar{p}$ mass threshold in $J/\psi \rightarrow \gamma\eta'\pi^+\pi^-$, *Phys. Rev. Lett.* **117**, 042002 (2016), arXiv:1603.09653 [hep-ex].
- [12] M. Ablikim *et al.* (BESIII), Study of $J/\psi \rightarrow \omega p\bar{p}$ at BESIII, *Phys. Rev. D* **87**, 112004 (2013), arXiv:1303.3108 [hep-ex].
- [13] G.-J. Ding and M.-L. Yan, Productions of X(1835) as baryonium with sizable gluon content, *Eur. Phys. J. A* **28**, 351 (2006), arXiv:hep-ph/0511186.
- [14] Z.-G. Wang and S.-L. Wan, X(1835) as a baryonium state with QCD sum rules, *J. Phys. G* **34**, 505 (2007), arXiv:hep-ph/0601105.
- [15] J. P. Dedonder, B. Loiseau, B. El-Bennich, and S. Wycech, On the structure of the X(1835) baryonium, *Phys. Rev. C* **80**, 045207 (2009), arXiv:0904.2163 [nucl-th].
- [16] X.-H. Liu, Y.-J. Zhang, and Q. Zhao, A Possible mechanism for producing the threshold enhancement in $J/\psi \rightarrow \gamma p\bar{p}$, *Phys. Rev. D* **80**, 034032 (2009), arXiv:0903.1427 [hep-ph].
- [17] B. S. Zou and H. C. Chiang, One-pion-exchange final-state interaction and the $p\bar{p}$ near threshold enhancement in $J/\psi \rightarrow \gamma p\bar{p}$ decays, *Physical Review D: Particles and Fields* **69**, 34004 (2004), arXiv:hep-ph/0309273.
- [18] A. Sibirtsev, J. Haidenbauer, S. Krewald, U.-G. Meißner, and A. W. Thomas, Near threshold enhancement of the $p\bar{p}$ mass spectrum in J/ψ decay, *Physical Review D: Particles and Fields* **71**, 54010 (2005), arXiv:hep-ph/0411386.
- [19] G. Y. Chen, H. R. Dong, and J. P. Ma, Rescattering Effect and Near Threshold Enhancement of $p\bar{p}$ System, *Phys. Rev. D* **78**, 054022 (2008), arXiv:0806.4661 [hep-ph].
- [20] G. Y. Chen, H. R. Dong, and J. P. Ma, Near Threshold Enhancement of $p\bar{p}$ System and $p\bar{p}$ Elastic Scattering, *Phys. Lett. B* **692**, 136 (2010), arXiv:1004.5174 [hep-ph].
- [21] G. Y. Chen and J. P. Ma, $N\bar{N}$ Scattering at NLO Order in An Effective Theory, *Phys. Rev. D* **83**, 094029

- (2011), [arXiv:1101.4071 \[hep-ph\]](#).
- [22] X.-W. Kang, J. Haidenbauer, and U.-G. Meißner, Near-threshold $\bar{p}p$ invariant mass spectrum measured in J/ψ and ψ' decays, *Phys. Rev. D* **91**, 074003 (2015), [arXiv:1502.00880 \[nucl-th\]](#).
- [23] B. A. Li, A Possible 0^{-+} glueball candidate X(1835), *Phys. Rev. D* **74**, 034019 (2006), [arXiv:hep-ph/0510093](#).
- [24] N. Kochelev and D.-P. Min, X(1835) as the lowest mass pseudoscalar glueball and proton spin problem, *Phys. Lett. B* **633**, 283 (2006), [arXiv:hep-ph/0508288](#).
- [25] G. Hao, C.-F. Qiao, and A.-L. Zhang, 0^{-+} triquion glueball and its implication for a recent BES observation, *Phys. Lett. B* **642**, 53 (2006), [arXiv:hep-ph/0512214](#).
- [26] N. Kochelev and D.-P. Min, Eta(c): Glueball mixing and resonance X(1835), *Phys. Rev. D* **72**, 097502 (2005), [arXiv:hep-ph/0510016](#).
- [27] L.-C. Gui, J.-M. Dong, Y. Chen, and Y.-B. Yang, Study of the pseudoscalar glueball in J/ψ radiative decays, *Phys. Rev. D* **100**, 054511 (2019), [arXiv:1906.03666 \[hep-lat\]](#).
- [28] T. Huang and S.-L. Zhu, X(1835): A Natural candidate of eta-prime's second radial excitation, *Phys. Rev. D* **73**, 014023 (2006), [arXiv:hep-ph/0511153](#).
- [29] J.-S. Yu, Z.-F. Sun, X. Liu, and Q. Zhao, Categorizing resonances X(1835), X(2120) and X(2370) in the pseudoscalar meson family, *Phys. Rev. D* **83**, 114007 (2011), [arXiv:1104.3064 \[hep-ph\]](#).
- [30] L.-M. Wang, Q.-S. Zhou, C.-Q. Pang, and X. Liu, Potential higher radial excitations in the light pseudoscalar meson family, *Phys. Rev. D* **102**, 114034 (2020), [arXiv:2010.05132 \[hep-ph\]](#).
- [31] Y.-F. Liu and X.-W. Kang, Status of X(1835) and $p\bar{p}$ Interaction from Chiral Symmetry, *Symmetry* **8**, 14 (2016).
- [32] B.-Q. Ma, Protonium: Discovery and Prediction, (2024), [arXiv:2406.19180 \[hep-ph\]](#).
- [33] K. Abe *et al.* (Belle), Observation of $B^{\pm} \rightarrow p\bar{p}K^{\pm}$, *Phys. Rev. Lett.* **88**, 181803 (2002), [arXiv:hep-ex/0202017](#).
- [34] K. Abe *et al.* (Belle), Observation of $\bar{B}^0 \rightarrow D^{0(*)}p\bar{p}$, *Phys. Rev. Lett.* **89**, 151802 (2002), [arXiv:hep-ex/0205083](#).
- [35] J. T. Wei *et al.* (Belle), Study of $B^+ \rightarrow p\bar{p}K^+$ and $B^+ \rightarrow p\bar{p}\pi^+$, *Phys. Lett. B* **659**, 80 (2008), [arXiv:0706.4167 \[hep-ex\]](#).
- [36] B. Aubert *et al.* (BaBar), A Study of $e^+e^- \rightarrow p\bar{p}$ using initial state radiation with BABAR, *Phys. Rev. D* **73**, 012005 (2006), [arXiv:hep-ex/0512023](#).
- [37] J. P. Lees *et al.* (BaBar), Study of $e^+e^- \rightarrow p\bar{p}$ via initial-state radiation at BABAR, *Phys. Rev. D* **87**, 092005 (2013), [arXiv:1302.0055 \[hep-ex\]](#).
- [38] R. R. Akhmetshin *et al.* (CMD-3), Study of the process $e^+e^- \rightarrow p\bar{p}$ in the c.m. energy range from threshold to 2 GeV with the CMD-3 detector, *Phys. Lett. B* **759**, 634 (2016), [arXiv:1507.08013 \[hep-ex\]](#).
- [39] G. Bardin *et al.*, Determination of the electric and magnetic form-factors of the proton in the timelike region, *Nucl. Phys. B* **411**, 3 (1994).
- [40] A. Antonelli *et al.*, Measurement of the electromagnetic form-factor of the proton in the timelike region, *Phys. Lett. B* **334**, 431 (1994).
- [41] A. Antonelli *et al.*, The first measurement of the neutron electromagnetic form-factors in the timelike region, *Nucl. Phys. B* **517**, 3 (1998).
- [42] R. R. Akhmetshin *et al.* (CMD-3), Observation of a fine structure in $e^+e^- \rightarrow$ hadrons production at the nucleon-antinucleon threshold, *Phys. Lett. B* **794**, 64 (2019), [arXiv:1808.00145 \[hep-ex\]](#).
- [43] M. Ablikim *et al.* (BESIII), Measurement of the proton form factor by studying $e^+e^- \rightarrow p\bar{p}$, *Phys. Rev. D* **91**, 112004 (2015), [arXiv:1504.02680 \[hep-ex\]](#).
- [44] M. Ablikim *et al.* (BESIII), Study of the process $e^+e^- \rightarrow p\bar{p}$ via initial state radiation at BESIII, *Phys. Rev. D* **99**, 092002 (2019), [arXiv:1902.00665 \[hep-ex\]](#).

- [45] M. Ablikim *et al.* (BESIII), Measurement of proton electromagnetic form factors in $e^+e^- \rightarrow p\bar{p}$ in the energy region 2.00 - 3.08 GeV, *Phys. Rev. Lett.* **124**, 042001 (2020), [arXiv:1905.09001 \[hep-ex\]](#).
- [46] M. Ablikim *et al.* (BESIII), Measurement of proton electromagnetic form factors in the time-like region using initial state radiation at BESIII, *Phys. Lett. B* **817**, 136328 (2021), [arXiv:2102.10337 \[hep-ex\]](#).
- [47] M. Ablikim *et al.* (BESIII), Oscillating features in the electromagnetic structure of the neutron, *Nature Phys.* **17**, 1200 (2021), [arXiv:2103.12486 \[hep-ex\]](#).
- [48] M. N. Achasov *et al.*, Study of the process $e^+e^- \rightarrow n\bar{n}$ at the VEPP-2000 e^+e^- collider with the SND detector, *Phys. Rev. D* **90**, 112007 (2014), [arXiv:1410.3188 \[hep-ex\]](#).
- [49] M. N. Achasov *et al.* (SND), Experimental study of the $e^+e^- \rightarrow n\bar{n}$ process at the VEPP-2000 e^+e^- collider with the SND detector, *Eur. Phys. J. C* **82**, 761 (2022), [arXiv:2206.13047 \[hep-ex\]](#).
- [50] M. N. Achasov *et al.*, Cross section of the process $e^+e^- \rightarrow n\bar{n}$ near the threshold, (2024), [arXiv:2407.15308 \[hep-ex\]](#).
- [51] J. Haidenbauer, H. W. Hammer, U.-G. Meißner, and A. Sibirtsev, On the strong energy dependence of the $e^+e^- \leftrightarrow p\bar{p}$ amplitude near threshold, *Phys. Lett. B* **643**, 29 (2006), [arXiv:hep-ph/0606064](#).
- [52] V. F. Dmitriev and A. I. Milstein, Final state interaction effects in the $e^+e^- \rightarrow N\bar{N}$ process near threshold, *Phys. Lett. B* **658**, 13 (2007).
- [53] J. Haidenbauer, X. W. Kang, and U. G. Meißner, The electromagnetic form factors of the proton in the timelike region, *Nucl. Phys. A* **929**, 102 (2014), [arXiv:1405.1628 \[nucl-th\]](#).
- [54] J. Haidenbauer, C. Hanhart, X.-W. Kang, and U.-G. Meißner, Origin of the structures observed in e^+e^- annihilation into multipion states around the $\bar{p}p$ threshold, *Phys. Rev. D* **92**, 054032 (2015), [arXiv:1506.08120 \[nucl-th\]](#).
- [55] V. F. Dmitriev, A. I. Milstein, and S. G. Salnikov, Real and virtual $N\bar{N}$ pair production near the threshold, *Phys. Rev. D* **93**, 034033 (2016), [arXiv:1512.00951 \[hep-ph\]](#).
- [56] A. I. Milstein and S. G. Salnikov, Fine structure of the cross sections of e^+e^- annihilation near the thresholds of $p\bar{p}$ and $n\bar{n}$ production, *Nucl. Phys. A* **977**, 60 (2018), [arXiv:1804.01283 \[hep-ph\]](#).
- [57] A. I. Milstein and S. G. Salnikov, $N\bar{N}$ production in e^+e^- annihilation near the threshold revisited, *Phys. Rev. D* **106**, 074012 (2022), [arXiv:2207.14020 \[hep-ph\]](#).
- [58] B. El-Bennich, M. Lacombe, B. Loiseau, and S. Wycech, Paris $N\bar{N}$ potential constrained by recent antiprotonic-atom data and antineutron-proton total cross sections, *Phys. Rev. C* **79**, 054001 (2009), [arXiv:0807.4454 \[nucl-th\]](#).
- [59] D. Zhou and R. G. E. Timmermans, Energy-dependent partial-wave analysis of all antiproton-proton scattering data below 925 MeV/c, *Phys. Rev. C* **86**, 044003 (2012), [arXiv:1210.7074 \[hep-ph\]](#).
- [60] T. Hippchen, J. Haidenbauer, K. Holinde, and V. Mull, Meson - baryon dynamics in the nucleon - anti-nucleon system. 1. The Nucleon - anti-nucleon interaction, *Phys. Rev. C* **44**, 1323 (1991).
- [61] V. Mull, J. Haidenbauer, T. Hippchen, and K. Holinde, Meson - baryon dynamics in the nucleon - anti-nucleon system. 2. Annihilation into two mesons, *Phys. Rev. C* **44**, 1337 (1991).
- [62] V. Mull and K. Holinde, Combined description of $\bar{N}N$ scattering and annihilation with a hadronic model, *Phys. Rev. C* **51**, 2360 (1995), [arXiv:nucl-th/9411014](#).
- [63] X.-W. Kang, J. Haidenbauer, and U.-G. Meißner, Antinucleon-nucleon interaction in chiral effective field theory, *JHEP* **02**, 113, [arXiv:1311.1658 \[hep-ph\]](#).
- [64] L.-Y. Dai, J. Haidenbauer, and U.-G. Meißner, Antinucleon-nucleon interaction at next-to-next-to-next-to-leading order in chiral effective field theory, *JHEP* **07**, 078, [arXiv:1702.02065 \[nucl-th\]](#).
- [65] Y. Xiao, J.-X. Lu, and L.-S. Geng, Antinucleon-nucleon interactions in covariant chiral effective field theory, (2024), [arXiv:2406.01292 \[nucl-th\]](#).

- [66] J. Carbonell, G. Hupin, and S. Wycech, Comparison of $N\bar{N}$ optical models, *Eur. Phys. J. A* **59**, 259 (2023), [arXiv:2309.14831 \[nucl-th\]](#).
- [67] K. M. Watson, The Effect of final state interactions on reaction cross-sections, *Phys. Rev.* **88**, 1163 (1952).
- [68] A. B. Migdal, Theory of nuclear reactions with formation of slow particles (1955).
- [69] X. Kong and F. Ravndal, Coulomb effects in low-energy proton proton scattering, *Nucl. Phys. A* **665**, 137 (2000), [arXiv:hep-ph/9903523](#).
- [70] E. Braaten, E. Johnson, and H. Zhang, Zero-range effective field theory for resonant wino dark matter. Part II. Coulomb resummation, *JHEP* **02**, 150, [arXiv:1708.07155 \[hep-ph\]](#).
- [71] P.-P. Shi, Z.-H. Zhang, F.-K. Guo, and Z. Yang, D^+D^- hadronic atom and its production in pp and $p\bar{p}$ collisions, *Phys. Rev. D* **105**, 034024 (2022), [arXiv:2111.13496 \[hep-ph\]](#).
- [72] X.-K. Dong, F.-K. Guo, and B.-S. Zou, Explaining the Many Threshold Structures in the Heavy-Quark Hadron Spectrum, *Phys. Rev. Lett.* **126**, 152001 (2021), [arXiv:2011.14517 \[hep-ph\]](#).
- [73] S. König, H. W. Griesshammer, H.-W. Hammer, and U. van Kolck, Effective theory of ^3H and ^3He , *J. Phys. G* **43**, 055106 (2016), [arXiv:1508.05085 \[nucl-th\]](#).
- [74] E. Braaten and M. Kusunoki, Factorization in the production and decay of the X(3872), *Phys. Rev. D* **72**, 014012 (2005), [arXiv:hep-ph/0506087](#).
- [75] A. M. Badalian, L. P. Kok, M. I. Polikarpov, and Y. A. Simonov, Resonances in Coupled Channels in Nuclear and Particle Physics, *Phys. Rept.* **82**, 31 (1982).
- [76] S. Sakai, F.-K. Guo, and B. Kubis, Extraction of ND scattering lengths from the $\Lambda_b \rightarrow \pi^- p D^0$ decay and properties of the $\Sigma_c(2800)^+$, *Phys. Lett. B* **808**, 135623 (2020), [arXiv:2004.09824 \[hep-ph\]](#).
- [77] F. James and M. Roos, Minuit: A System for Function Minimization and Analysis of the Parameter Errors and Correlations, *Comput. Phys. Commun.* **10**, 343 (1975).
- [78] H. Dembinski *et al.*, *iminuit*: A python interface to minuit, <https://github.com/scikit-hep/iminuit>.
- [79] F.-K. Guo, *IMinuit.jl*: A julia wrapper of iminuit, <https://github.com/fkguo/IMinuit.jl>.
- [80] Z.-H. Zhang and F.-K. Guo, Classification of Coupled-Channel Near-Threshold Structures, (2024), [arXiv:2407.10620 \[hep-ph\]](#).
- [81] R. J. Eden and J. R. Taylor, Poles and Shadow Poles in the Many-Channel S Matrix, *Phys. Rev.* **133**, B1575 (1964).